A Dual-Polarized SIW Lens Antenna Array for Rx-/Tx-Integration at K/Ka-Band

Thomas Jaschke and Arne F. Jacob, *Life Fellow, IEEE*

***Abstract*— The terminal antenna with dual-circular polarization reported here operates around 20 and 30 GHz, that is, in the down- and uplink frequency bands of current satellite communication systems. The passive array, this work focuses on, integrates the receive and the transmit (Rx/Tx) paths in a single aperture. This approach is shown to be advantageous compared to classical solutions with two separate antennas. The modules, the array consists of, are formed by a stack of eight linear subarrays that themselves are composed of an alternating series of four Tx-only and four combined Rx/Tx endfire antenna elements. The resulting brick architecture provides enough real estate for the future implementation of phased-array electronics. The array is implemented in substrate-integrated waveguide (SIW) technology. For improved matching, it is covered with a periodically shaped dielectric lens. A technique is proposed to mitigate cross-polarization in the pointing direction. A module is realized using standard technologies. The relevant array parameters are measured. The module patterns are synthesized from the individual element responses. They confirm the simulated results and, in particular, a bandwidth of more than 2.5 GHz for both Rx and Tx.**

***Index Terms*— Circular polarization, K-/Ka-band, lens antenna, phased array, receive (Rx)/transmit (Tx) integration, substrate-integrated waveguide (SIW).**

I. Introduction

HIGH-SPEED Internet access is nowadays available even in remote areas via high-throughput Ka-band satellites in the geostationary orbit [1], [2]. In mobile scenarios, right-handed circular polarization (RHCP) and left-handed circular polarization (LHCP) are often used in combination with the four-color spot-beam scheme [3]. The allocated down- and uplink frequency bands range from 18.7 to 21.2 GHz for receive (Rx) and from 27.5 to 30 GHz for transmit (Tx). The subbands utilized within these are regulation- or service-dependent.

Manuscript received 27 May 2022; revised 2 December 2022; accepted 11 December 2022. Date of publication 19 January 2023; date of current version 6 March 2023. This work was supported by the German Space Agency at DLR (German Aerospace Center) on behalf of the German Federal Ministry of Economics and Technology (BMWi) under Grant 50YB1707. *(Corresponding author: Thomas Jaschke.)*

Thomas Jaschke was with the Institute of High-Frequency Technology, Hamburg University of Technology, 21073 Hamburg, Germany. He is now with Wärtsilä Voyage GmbH, 22761 Hamburg, Germany (e-mail: jaschke@tuhh.de).

Arne F. Jacob is with the Institute of High-Frequency Technology, Hamburg University of Technology, 21073 Hamburg, Germany (e-mail: jacob@tuhh.de).

Color versions of one or more figures in this article are available at https://doi.org/10.1109/TAP.2023.3235006.

Digital Object Identifier 10.1109/TAP.2023.3235006

In these applications, terminal antennas have to generate a steerable pencil beam. Despite requiring several thousand elements [4], arrays are nowadays often preferred over reflector antennas because of their higher beam scanning agility and their potentially lower profile. Because of the large frequency spread between them, the Rx and the Tx bands are often served by two separate arrays [5], [6], [7], [8], albeit integrating the Rx/Tx functionality in a single aperture could possibly reduce the overall size. In this case, which is referred to as Rx/Tx integration in the following, the specific frequency spread considered here allows for interleaved rectangular array grids with Tx-only and combined Rx/Tx elements [9], [10]. The development of dual-band, dual-polarized antenna elements with sufficient bandwidth is a major challenge, though.

The tile architecture [11, Sec. 1.3.1] is commonly encountered in planar arrays. Antennas featuring either dual-polarization or dual-band operation are presented in [12] and [13], [14], and [15], respectively. Solutions combining both properties have also been proposed, for example, by Greco et al. [16] who simulate two nested annular slot elements. Stacked microstrip patches fed by two crossed aperture-coupled feed lines are demonstrated in [17] and [18]. However, these solutions are rather narrowband. Wideband antennas are better suited to handle multiple bands in a single aperture. Examples are tightly coupled dipoles, which are ultrawideband [19], [20]. A drawback of this concept is the associated small element spacing which increases the number of elements and, in turn, the integration density especially of the electronic circuitry. Thus, implementing Rx/Tx functionality and dual-polarization becomes a tremendous packaging challenge.

The brick architecture [11, Sec. 1.3.1] may relieve this problem. Recent examples of tightly coupled dipoles [21] and Vivaldi antennas [22] show the potential. However, they rely on crossed printed circuit boards (PCBs) to realize dual-polarization, which results in mechanically complicated setups. Classical waveguides, on the other hand, offer many advantages, such as large bandwidth, dual-polarization capability, low losses, and good element isolation [23], [24], [25]. In general, however, they are bulky and expensive.

This can be remedied by the substrate-integrated waveguide (SIW) technology, which combines waveguides and planar fabrication techniques. This reduces manufacturing costs while maintaining most of the advantages of waveguides. The concept was demonstrated in [26] and [27], which report a dual-polarized endfire array based on square SIWs. The aperture is matched by means of a choke, which, however,

is relatively narrowband and does not support dual-band operation. Dielectric lenses are a promising alternative. They are usually applied to improve the input match or to shape the radiation pattern [28], [29], [30], [31]. In [32], [33], and [34], they terminate a dual-polarized endfire SIW antenna to achieve wideband matching at K-/Ka-band.

Following the above discussions, this contribution aims at demonstrating the feasibility of a passive endfire SIW array terminated by a dielectric lens, as shown in Fig. 1. The antenna shall integrate the Rx and the Tx paths in a single aperture and, in contrast to [35], support dual-polarization in both. It should operate at least in the 0.5 GHz wide bands from 19.7 to 20.2 GHz for Rx and from 29.5 to 30 GHz for Tx, as these are globally available and supported by most of the K-/Ka-band satellites. They will be labeled *reference* from now on. In addition, of course, the performance achieved in the 2.5 GHz wide Rx and Tx bands, mentioned previously and referred to as *typical* in the following, is also of strong interest and shall be considered.

The remainder of this article is organized as follows. Section II introduces the antenna concept, presents a method to mitigate cross-polarization, and evaluates the surface area savings compared to the case of two separate Rx and Tx arrays. Section III deals with the design of the antenna aperture, that is, of the SIWs and the dielectric lens, and reports the simulated performance. It also describes the design of the whole array, including, in particular, the feeds and the septum polarizers. Section IV, finally, presents the realization and discusses the experimental results.

II. Rx/Tx Integrated Array Concept

A. Basic Array Element

As mentioned above, the array is composed of dual-polarized endfire SIW antennas terminated by a dielectric lens. The dual-band design detailed in [32] and [34] is suitable here. Its main features are summarized below. Fig. 2 recalls the basic concept. The square SIW in Fig. 2(a) supports two fundamental degenerated modes, which, by superposition, can yield any polarization, in particular, also RHCP and LHCP. It consists of a standard PCB sandwiched between two superstrates and an outer copper layer. It is further matched by means of a shaped dielectric lens (see Fig. 2(b)). Because of their reduced height, the two standard SIWs with ports P1 and P2 on the left only support linear polarization. An E-plane taper realizes the transition between them and the square SIW [32], [34]. The output of the latter circular polarization is obtained by means of a septum polarizer [36], [37], [38] when driving either P1 or P2. The thinner layer stack on the left leaves enough space in the vertical (y-)direction to accommodate diplexers, active front-end circuitry, and thermal management gear.

Based on this previous work, the Rx/Tx integrated element needs to be adapted to the array environment, whereas the Tx-only antenna still remains to be designed.

B. Array Grid

As illustrated in Fig. 3(a), the Tx-only and the combined Rx/Tx elements are arranged in an interleaved rectangular grid, as this minimizes the number of front-end channels per surface area [10]. To prevent grating lobes, the elements are $d_{Rx} = 7.1$ mm and $d_{Tx} = 5$ mm apart. This corresponds to half a wavelength at 21.2 and 30 GHz, respectively. In the modular approach pursued in this work, the two antenna types are alternated to form linear subarrays. These are stacked to modules with adjustable sizes.

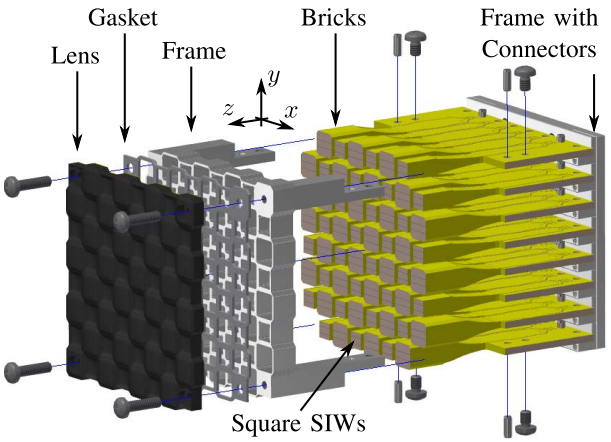

Fig. 1. Exploded view of the lens antenna array.

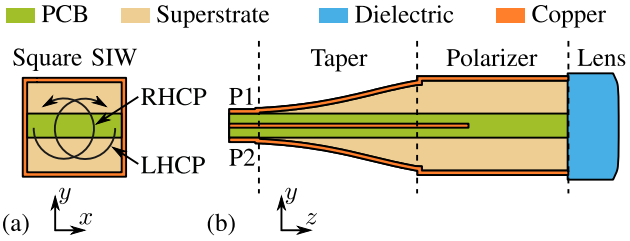

Fig. 2. Schematic of the lens antenna concept. (a) Cross and (b) longitudinal section.

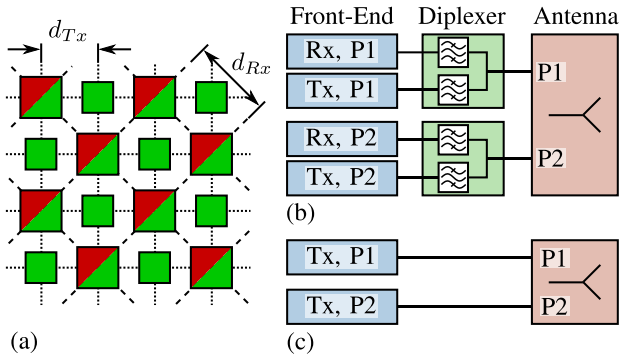

Fig. 3. (a) Interleaved rectangular array grid for an Rx/Tx integrated aperture (■ Rx/■ Tx element, ... grid lines). Schematic of (b) Rx/Tx and (c) Tx-only antenna elements with dual-polarization (P1/P2).

C. Front-End Architecture

Albeit this work focuses on the passive part of the array, the ultimate goal is to realize a phased array. Therefore, also the front-end architecture has to be considered to verify that it does not inhibit the feasibility of the approach.

Fig. 3(b) and (c) shows a possible setup, with each polarization representing a separate path calling for its own connection. Whereas Tx-only elements are directly routed to the front ends, the combined Rx/Tx antennas require diplexers in

between. These have to provide enough isolation between Tx and Rx to prevent receiver saturation [39]. More importantly, the insertion loss must be minimized. Suitable solutions were proposed in [40] and [41]. A complete setup employing the core chips *AWS-0102* and *AWMF-0109* from *Anokiwave* as beamformers and the low-noise amplifier (LNA) *QPA2626* from *Qorvo* was demonstrated in [42], [43], and [44]. As, in particular, it satisfies the spatial requirements of the array grid, it could be a suitable solution in the present context.

D. Polarization Compensation

If the polarizers were ideal and the antennas perfectly symmetric, the far field would be circularly polarized at boresight. In other directions, the wave is depolarized and cross-polarization rises. This effect can be minimized by an appropriate antenna design. In practice, however, this cannot be achieved for all pointing directions and over wider frequency bands. In array applications, the copolarization in the pointing direction (θ_0, ϕ_0) is of major interest. As shown in the following, the cross-polarization can be compensated by the second polarization ports, which are available in the proposed array concept. The array far fields $\vec{g}_1$ and $\vec{g}_2$ in (θ_0, ϕ_0) are measured with an excitation at the ports P1 and P2. A weighted superposition yields

$$\vec{g} = [g] \begin{bmatrix} \alpha_1 \\ \alpha_2 \end{bmatrix} \quad \text{with} \quad [g] = \left[\vec{g}_1(\theta_0, \phi_0)\ \vec{g}_2(\theta_0, \phi_0) \right]. \tag{1}$$

The complex weighting coefficients α_p with $p = 1, 2$ are normalized according to $|\alpha_1|^2 + |\alpha_2|^2 = 1$ and the far fields $\vec{g}_p$ are collected in the matrix $[g]$. With $\vec{e}_{pol}$ the unit vector of the intended polarization, the desired far field can be written as

$$\vec{g} = |\vec{g}|\, \vec{e}_{pol}. \tag{2}$$

With (1), this yields the required weighting coefficients

$$\begin{bmatrix} \alpha_1 \\ \alpha_2 \end{bmatrix} = [g]^{-1}\, \vec{g} = |\vec{g}|\, [g]^{-1}\, \vec{e}_{pol}. \tag{3a}$$

The far-field magnitude is given by

$$|\vec{g}| = \left| [g]^{-1}\, \vec{e}_{pol} \right|^{-1} \tag{3b}$$

from a comparison of the magnitudes in (3a). The approach fails, when $[g]$ is singular and, thus, the far fields $\vec{g}_p$ are linearly dependent. In general, the condition number of the linear system [45, Sec. 50.5] is a measure for the necessary accuracy of the weighting coefficients α_p and the knowledge of the gain matrix $[g]$. It is highest for orthogonal fields $\vec{g}_p$.

To implement this compensation technique, the beamformer must be able to control the amplitude and phase of both polarizations simultaneously. Additionally, in general, the excitation varies for the different pointing directions, which have to be considered in the implementation. A further feature of this approach is that any (e.g., also linear) polarization can be generated.

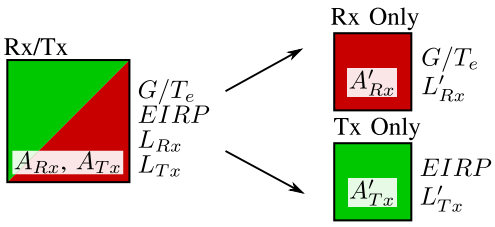

Fig. 4. Schematic of integrated and separate array antennas.

E. Surface Area Comparison

1) Scaling Relations: As the implementation effort associated with the proposed integration is substantial, it is mandatory to assess its potential benefit, that is, mainly the savings in terms of total surface area compared to the case of separate antennas. As sketched in Fig. 4, the following assumes identical equivalent isotropically radiated power (EIRP) and gain-to-noise temperature (G/T). The differences, which stem from the additional losses introduced by the diplexers and the longer transmission lines needed in the integrated solution, have to be compensated by a larger surface area.

In the following, surface areas are denoted as A, losses as L, antenna gains as G, system noise temperatures as T_e, and drive powers (per antenna element) as P (P_{ele}). The subscripts Rx and Tx refer to the function, the primed quantities to the separate arrays, and the unprimed ones to the Rx/Tx integrated case. These quantities scale as

$$X' = \Delta X\, X \tag{4}$$

with $X \in \{A_{Rx}, A_{Tx}, L_{Rx}, L_{Tx}, G_{Rx}, G_{Tx}, T_e, P, P_{ele}\}$.

As the gain of an array is proportional to the surface area and inversely proportional to the antenna losses, (4) leads to

$$\Delta G_{Rx} = \frac{\Delta A_{Rx}}{\Delta L_{Rx}} \quad \text{and} \quad \Delta G_{Tx} = \frac{\Delta A_{Tx}}{\Delta L_{Tx}}. \tag{5}$$

Again with (4) and for identical G/T_e in the Rx case, this yields

$$\frac{\Delta G_{Rx}}{\Delta T_e} = \frac{\Delta A_{Rx}}{\Delta L_{Rx}\, \Delta T_e} = 1 \tag{6a}$$

and, thus,

$$\Delta A_{Rx} = \Delta L_{Rx}\, \Delta T_e. \tag{6b}$$

In the Tx case, the total drive power is proportional to the (mean) drive power per element and to their number, that is, finally to the surface area of the array. For identical EIRP, defined as the product of total drive power and Tx gain, and from (4), it follows that

$$\Delta P\, \Delta G_{Tx} = \Delta A_{Tx}^2\, \frac{\Delta P_{ele}}{\Delta L_{Tx}} = 1 \tag{7a}$$

and, thus

$$\Delta A_{Tx} = \sqrt{\frac{\Delta L_{Tx}}{\Delta P_{ele}}}. \tag{7b}$$

The element power P_{ele} is limited either by the employed circuit or, for a given number of array elements, by EIRP regulations. For satellite communications, the European Telecommunications Standards Institute (ETSI) defines a mask for the maximum allowable EIRP at 2° off the pointing direction [46].

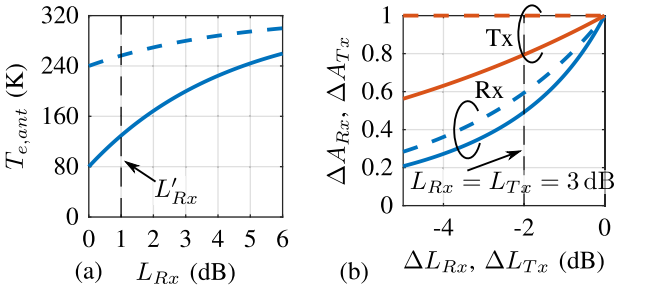

Fig. 5. (a) Equivalent antenna noise temperature versus antenna loss and (b) area factors versus ΔL_{Rx} or ΔL_{Tx} (— clear sky, - - heavy rain, — ΔA_{Tx} for $\Delta P_{ele} = 1$, and - - ΔA_{Tx} for $\Delta P_{ele} = \Delta L_{Tx}$).

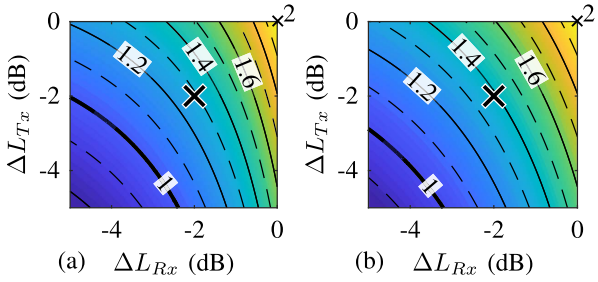

Fig. 6. Contour plot of the total surface area factor ΔA versus ΔL_{Rx} and ΔL_{Tx} for (a) clear sky and (b) heavy rain scenario (✖ $\Delta L_{Rx} = \Delta L_{Tx} = -2$ dB).

2) Results: The equivalent system noise temperature at the receiver input is given by

$$T_e = T_{e,r} + T_{e,ant} \tag{8a}$$

with

$$T_{e,r} = T_0 \left(F_r - 1\right) \tag{8b}$$

the equivalent input receiver noise temperature and

$$T_{e,ant} = \frac{T_{ant}\left(L_{Rx} - 1\right) + T_{e,0}}{L_{Rx}} \tag{8c}$$

the equivalent antenna noise temperature. In the above, F_r is the receiver noise figure, $T_0 = 290$ K is the reference temperature, $T_{e,0}$ is the noise received by the antenna, and T_{ant} its physical temperature [47, Eq. (10.15)].

The following analysis is conducted for $T_{e,0} = 80$ K and 240 K for clear sky and heavy rain, respectively. With $T_{ant} = 320$ K, this yields the $T_{e,ant}$ dependence on L_{Rx} plotted in Fig. 5(a). The increase is substantial and more pronounced for a clear sky. The receiver noise figure of $F_r = 1.5$ dB assumed here yields $T_{e,r} = 120$ K. It is achievable with state-of-the-art LNAs.[1] Finally, L'_{Rx} and L'_{Tx} are set to 1 dB, which are reasonable values in view of the short connections realizable in separate arrays. Fig. 5(b) shows how the Rx and Tx surface areas scale with the differences in antenna loss.

Assuming the additional losses in the Rx/Tx integrated array to result in $\Delta L_{Rx} = \Delta L_{Tx} = -2$ dB, this yields $\Delta A_{Rx} = 0.49$ and 0.59 in the two considered weather scenarios. For Tx, two cases have to be considered.

1) The EIRP is limited by the ETSI mask. Then, for identical EIRP, the surface areas are identical and $\Delta A_{Tx} = 1$. In turn, P'_{ele} has to be reduced, yielding $\Delta P_{ele} = \Delta L_{Tx}$.
2) The EIRP is limited by the available element power. Then, $\Delta P_{ele} = 1$ and ΔA_{Tx} depends on ΔL_{Tx}, as reported in Fig. 5(b). With $\Delta L_{Tx} = -2$ dB, $\Delta A_{Tx} = 0.79$ is achievable.

In general, the additional Rx losses have a stronger impact than the Tx ones, as visible in the graphs of Fig. 5(b).

In the following, the integrated array is assumed to satisfy $A_{Tx} = A_{Rx} = A$. Then, the factor $\Delta A = \Delta A_{Rx} + \Delta A_{Tx}$ is a measure of the realizable savings in surface area. Fig. 6 reports its dependencies on ΔL_{Rx} and ΔL_{Tx} for the two weather scenarios. Here, it is assumed that the EIRP is not limited by the ETSI mask. The optimum case with $\Delta L_{Rx} = \Delta L_{Tx} = 0$ dB yields $\Delta A = 2$. As losses increase, ΔA decreases, until, for $\Delta A = 1$, the integrated solution is no longer advantageous. For $\Delta L_{Rx} = \Delta L_{Tx} = -2$ dB, ΔA reaches 1.29 and 1.39 for the two weather scenarios. This even increases to 1.49 and 1.59, when the EIRP is limited by the ETSI mask.

In conclusion, provided the additional losses remain low enough—which is a quite realistic prospect according to the state of the art—the Rx/Tx integrated solution outperforms the case with separate Rx and Tx arrays.

III. Dual-Polarized Lens Array Design

This section reports the design and the realization of a complete module of the passive array. It first discusses the layout of the aperture, which consists of a shaped dielectric lens covering square K- and Ka-band SIWs, and then describes its combination with the polarizers.

A. Aperture With Lens

The SIWs are arranged as sketched in the top view in Fig. 3(a). In the cross section in Fig. 7(a), one recognizes the shaped lens and the two types of SIWs, together with the relevant dimensions. Here, and in the following, the subscripts 1 and 2 are attributed to the Rx/Tx and the Tx-only elements, respectively.

1) Design Goals: To realize circular polarization and wideband matching with low dispersion, the width a_n and the height b_n of the SIW should be chosen so that the (vertical) TE_{10}- and (horizontal) TE_{01}-modes are degenerated and sufficiently far above the cutoff in the intended operating frequency range. They may differ somewhat, though, as the employed substrate materials may be anisotropic.

The lens is intended to act as an impedance transformer. Its thickness is approximately a quarter wavelength and, thus, different depending on the SIW it covers. The smoothness of the resulting transitions should be adjustable to minimize parasitic edge effects.

2) Design Approach: Fourth-order nonuniform rational basis splines (NURBSs) [48] are an adequate and convenient means to describe the lens surface with sufficient smoothness. As shown in Fig. 7(b), they are defined by means of 16 supporting points per element arranged on two concentric polygons above each SIW, yielding a fourth-order rotational symmetry and mirror symmetries with respect to the xz- and

[1]See, for example, LNA *QPA2626* from *Qorvo*.

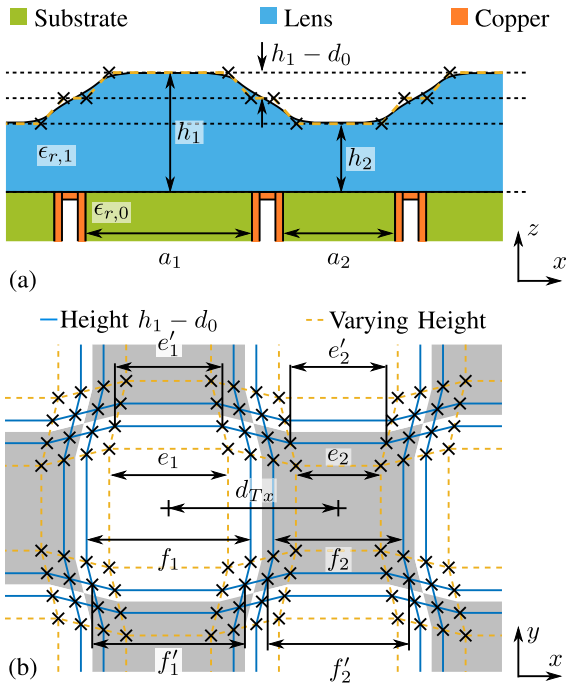

Fig. 7. (a) Cross section and (b) parameterized lens surface.

yz-planes. The inner polygons (here squares) and the outer ones are placed on planes at height h_n and $h_1 - d_0$, respectively. The side lengths are given by

$$e'_n = e_n - \alpha\,(e_n - e_{3-n})/2 \tag{9a}$$

$$f_n = e_n + \alpha\,(d_{Tx} - (e_1 + e_2)/2) \tag{9b}$$

and

$$f'_n = f_n - \alpha\,(f_n - f_{3-n})/2. \tag{9c}$$

Parameter α determines the position of the intermediate supporting points, which varies between the edges of the central squares defined by e_n ($\alpha = 0$) and the center of the transition between them ($\alpha = 1$). Larger α yields a smoother surface.

To fine-tune the smoothness, the four supporting points defined by f_n (f'_n) are weighted with w_0 (w'_0). Larger weights draw the surface closer toward the supporting points. Likewise, the points at the heights h_n are provided with weighting factors w_n.

The lens surface is optimized by systematically varying the design parameters. To reduce their number, some of them are fixed beforehand by selecting the materials and through prior investigations. The main idea is that the pattern of the lens corresponds to the shape of the SIWs, whereby its surface should be relatively flat above them. The lens consists of *Rogers' Duroid 5880* with permittivity $\epsilon_{r0} = 2.2$, the SIWs of *Panasonic's Megtron 6* with permittivity $\epsilon_{r1} = 3.65$ in-plane (xz) and 3.38 out-of-plane (yz). With this, the dimensions of the SIW are set to $a_1 = 4.8$ mm, $a_2 = 3.2$ mm, $b_1 = 4.6$ mm, and $b_2 = 3.1$ mm. The corners of the Rx/Tx SIW are chamfered by 0.5 mm to leave more space between diagonal elements (see Fig. 8). This yields the cutoff frequencies f_c and effective permittivities $\epsilon_{r,eff}$ listed in Table I. Due to the 2.8 μm surface roughness of the copper cladding, the latter are slightly larger than the corresponding substrate values.

TABLE I
CHARACTERISTICS OF THE SIW MODES

m	Mode	f_c (GHz)		$\epsilon_{r,eff}$		Symmetry[3,4]	
		SIW 1	SIW 2	SIW 1	SIW 2	xz-Plane	yz-Plane
1[1]	TE_{01}	16.8	24.3	3.91	3.91	PEC	PMC
2[2]	TE_{10}	16.7	24.4	3.64	3.63	PMC	PEC
3	TM_{11}	22.8	-	3.85	-	PMC	PMC
4	TE_{11}	24.1	-	3.70	-	PMC	PMC

[1] Horizontal mode. [2] Vertical mode. [3] Perfect electric conductor (PEC). [4] Perfect magnetic conductor (PMC).

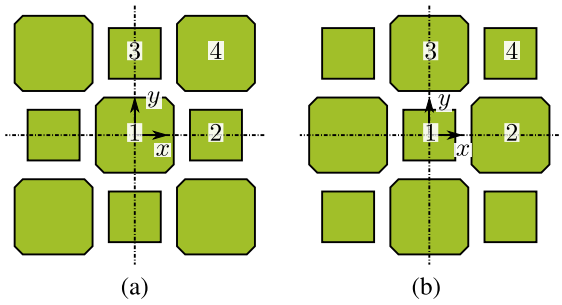

Fig. 8. Simulation models with (a) Rx/Tx and (b) Tx-only element at the center.

To obtain a relatively flat lens above the SIWs, the following choices are made: $e_1 = 4.5$ mm, $e_2 = 3.1$ mm, $\alpha = 0.2$, $w_1 = w_2 = 5$, $w_0 = 1$, and $w'_0 = 0.2$. As a result, the transitions are quite steep, yet smooth due to the NURBS. The remaining three parameters h_1, h_2, and d_0 are varied systematically.

To minimize the computational effort, the study is carried out with the smallest possible simulation setup, that is, the two 3×3 arrays with infinite ground plane sketched in Fig. 8. They approximate the array environment for the central element, which is either an Rx/Tx or a Tx-only antenna. The far-field patterns, the input reflections, and the interelement coupling are computed[2] by successively exciting the central element with the modes listed in Table I. The model size is further reduced by utilizing the symmetries listed in Table I. The antenna elements are numbered as shown in Fig. 8.

3) Results: The array performance is assessed in the *typical* frequency bands (see Section I) through two parameters, namely the maximum input reflection Γ_{max} and the ratio of maximum to minimum directivity $D_{rel} = D_{max}/D_{min}$ in the boresight direction. The latter is a measure of the directivity flatness over frequency [33]. As these parameters are different for the two antenna elements and mode combinations, only a single value is retained to evaluate the performance. For Γ_{max}, the maximum overall value is chosen, and, for D_{rel}, the variation is determined from the maximum and the minimum element directivity of all element and mode combinations.

The systematic parameter study yields the contour plots in Fig. 9. The selected geometry with $h_1 = 2.6$ mm, $h_2 = 1.8$ mm, and $d_0 = 0.3$ mm is marked by crosses. The achieved $\Gamma_{max} = -16.2$ dB and $D_{rel} = 1.8$ dB represent a good compromise.

Fig. 10 provides more insights by reporting the scattering parameters $S_{\bar{n}[\bar{m}],1[m]}$. Here, the subscripts $\bar{n}$ and 1 refer to the elements and $\bar{m}$ and m to the modes (see

[2] Throughout with *CST Microwave Studio*.

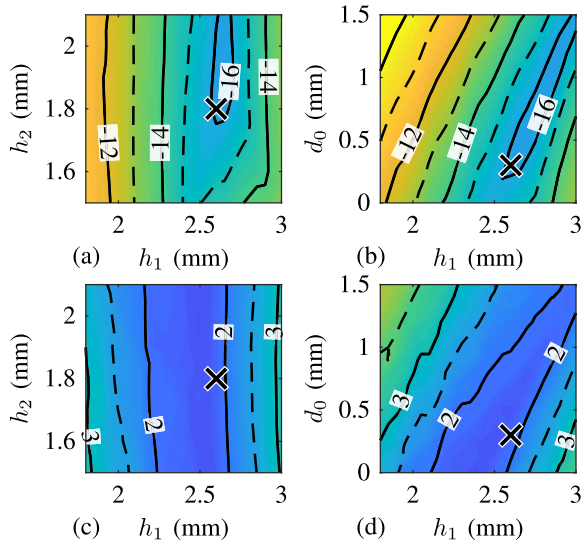

Fig. 9. (a) Γ_{max} and (c) D_{rel} versus h_1 and h_2 ($d_0 = 0.3$ mm). (b) Γ_{max} and (d) D_{rel} versus h_1 and d_0 ($h_2 = 1.8$ mm).

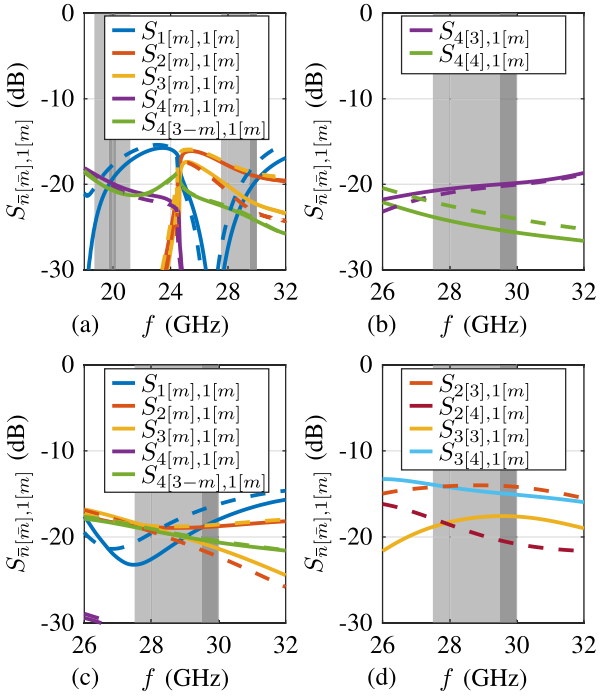

Fig. 10. Simulated scattering parameters of the array (a) and (b) from Fig. 8(a) and (c) and (d) from Fig. 8(b). (a) and (c) fundamental mode case and (b) and (d) higher-order mode case (▬ horizontal ($m = 1$), ▪ ▪ vertical ($m = 2$), ■ *typical*/■ *reference* bands).

Table I). Fig. 10(a) and (b) shows the results for the model of Fig. 8(a). The input reflection $S_{1[m],1[m]}$ and the coupling coefficients $S_{\bar{n}[\bar{m}],1[m]}$ are very low in both frequency bands. The Γ_{max}-value of -16.2 dB is determined by the TE_{10} mode in the Rx band. The strongest coupling (-18.8 dB) occurs between elements 1 and 4. In the Tx band, the elements 2 and 3 operate above the cutoff. The resulting couplings, including those to higher-order modes, remain below -17.2 dB. Fig. 10(c) and (d) shows the results for the model of Fig. 8(b). The input reflection is acceptably low here too (Γ_{max} is defined by the Rx/Tx element). The fundamental mode coupling between elements peaks at -18.3 dB, whereas

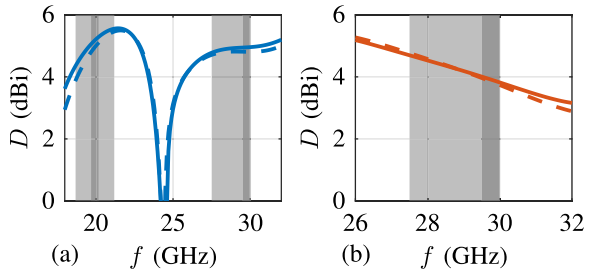

Fig. 11. Directivity D for (a) Rx/Tx and (b) Tx-only element (▬ horizontal ($m = 1$), ▪ ▪ vertical ($m = 2$), ■ *typical*/■ *reference* bands).

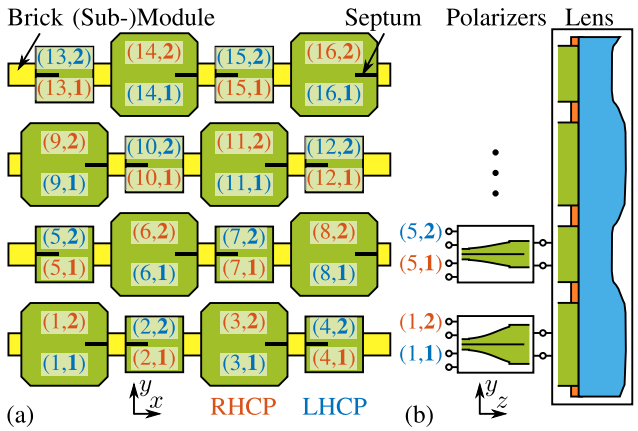

Fig. 12. (a) Top-view and port numbering of the central SIW feeds. (b) Equivalent circuit of the lens array antenna.

the higher-order modes of element 2 and 3 are coupled by up to -14 dB when driving antenna 1.

The directivity, plotted in Fig. 11, varies between 3.9 and 5.6 dBi (3.7 and 4.8 dBi) for the Rx/Tx (Tx-only) element in the *typical* frequency bands. The directivity is relatively flat in the assessed frequency bands with $D_{rel} = 1.8$ dB.

B. Lens Antenna Array With Polarizers

1) Design Goals: A dual-polarized 8 × 8 lens array, that is, with 32 Tx-only and 32 Rx/Tx antenna elements, serves as a demonstrator. It consists of eight submodules with eight elements each. To mitigate edge effects, the outer elements are terminated, effectively leaving an undisturbed 4 × 4 array. To achieve dual-polarization, the aperture reported in Section III-A is combined with septum polarizers. These follow the design of [32] but have to be adapted for the material stack used here. For the Rx/Tx element, they cover the *typical* frequency bands. In the case of the Tx-only element, they have yet to be designed.

Fig. 12(a) is a top view of the SIWs feeding the central 4 × 4 array. Each element n has two input ports (n,**1**) and (n,**2**) to accommodate LHCP and RHCP. The position of the polarizer septum alternates between the right and the left sides to improve the symmetry of the array pattern. The polarizer inputs change accordingly.

2) Modeling: A full-wave simulation of the whole array could not be conducted with the available computer resources. To overcome this, the array is first simulated without polarizers and then combined with them through an equivalent circuit, as sketched in Fig. 12(b). For this, the scattering

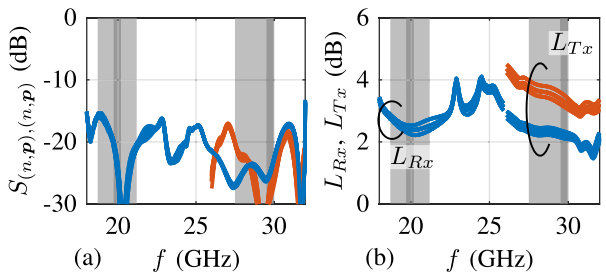

Fig. 13. Simulated (a) input reflections and (b) antenna losses L_{Rx} and L_{Tx} of the Rx/Tx and Tx-only elements (*typical*/*reference* bands).

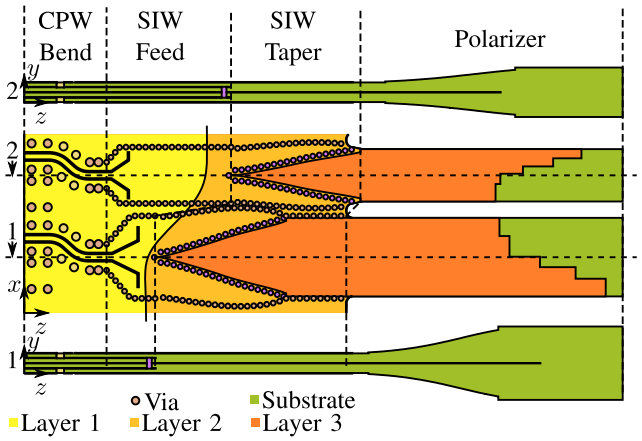

Fig. 14. Schematic top view and cross sections of the PCB with a Tx-only and an Rx/Tx element.

parameters and the element far-field patterns are calculated for the fundamental and, where meaningful, for the higher-order propagating modes by full-wave simulation. They are then combined with the simulated full-wave responses of the polarizers. Here, the coupling through the square SIWs due to evanescent modes is neglected and, thus, the array characteristics are only approximated by the equivalent circuit model.

3) Results: Fig. 13(a) reports the input reflections of the individual array elements. They are quite similar for elements of the same type. For the Rx/Tx antennas, they peak at −15.3 and −22.6 dB in the *typical* Rx and Tx bands, respectively, and for the Tx-only elements at −20 dB. Fig. 13(b) depicts the losses, which are particularly relevant in the present context (see discussion in Section II-E). In the *typical* band, L_{Rx} ranges between 2.2 and 2.9 dB and L_{Tx} between 2.1 (3) and 2.5 dB (4 dB) for the Rx/Tx (Tx-only) element. In the *reference* bands, which are most relevant in practice, these numbers become $L_{Rx} = 2.4$ dB, $L_{Tx} = 2.2$ dB (Rx/Tx element), and $L_{Tx} = 3.3$ dB (Tx-only element). Other array properties, like mutual coupling and far-field characteristics, are discussed in Section IV-B together with the measurement results.

IV. Array Demonstrator

A. Realization

1) Manufacturing Steps: Fig. 14 shows the PCB layout of two neighboring antenna elements. Their interface to the measurement equipment are SMPS connectors (*3811-40003* from *SV Microwave*) soldered to coplanar waveguides (CPWs)

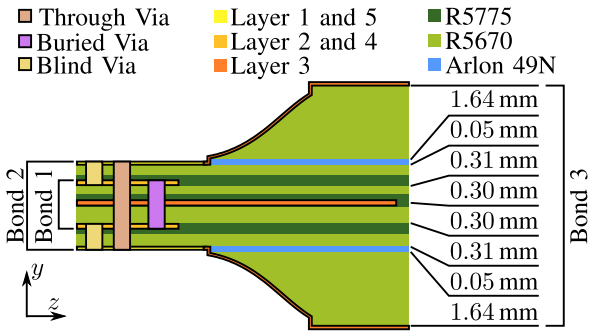

Fig. 15. Layer stack of the array.

on each side of the layer stack. To accommodate them within the limited available space, the CPWs incorporate a bend. Combinations of CPW-to-SIW transitions [49] and SIW tapers [50] realize broadband connections with the polarizer inputs. The overall length of the PCB is 37 mm. Fig. 15 depicts the layer stack of *Megtron 6* series laminates and prepregs.

The following details the manufacturing steps.

1) The inner stack with five metal layers (see Fig. 16(a)) is manufactured in a standard PCB process, which requires two bond cycles to realize buried, blind, and through vias. The structure is almost symmetric with respect to the layer 3, which contains the polarizer septa.
2) The *Megtron 6* superstrates on both sides are bonded using shaped, low-flow *Arlon 49N* prepregs with controlled flow properties (see Fig. 16(b)). This is important to prevent them from spilling over the outer metal layers.
3) The PCB including the superstrates are machined from both sides with a three-axis miller (see Fig. 16(c)), starting with the upper side of the SIWs with the two different heights. Then, the tapers of the polarizers are milled stepwise from the top to the inner PCB. Finally, the sidewalls of the SIWs and the chamfered edges are machined with an end and a chamfer mill, respectively.
4) A Kapton film (*Nitto P-221*) is applied on the outer metal layers to protect them.
5) The PCB is metalized by chemically depositing a copper layer that is galvanically reinforced to 17 μm. After removing the Kapton, copper is treated with the silver (improve conductivity) and the gold (prevent oxidation) immersion processes from *Hofstetter*.
6) Finally, unplated holes are drilled, and the submodules are milled out (see Fig. 16(d)).

Eight such submodules are mounted in an aluminum frame, which also supports the 32 SMPS connectors. The unused ports are terminated by surface-mounted device (SMD) resistors (*CH02016-50RGFT* from *Vishay*). The lens is milled into a 2.6 mm-thick *Duroid 5880* substrate. The back-metallization is selectively removed to match the SIW apertures (see Fig. 17(a)). A second aluminum frame maintains the submodules and the lens. It features apertures to accommodate the SIW antennas. Four screws at the corners fix the lens, thus disabling the array elements there. A gasket between the frame and lens ensures the required galvanic contact with the SIWs. It is fabricated from a 0.5 mm-thick conductive silicone rubber

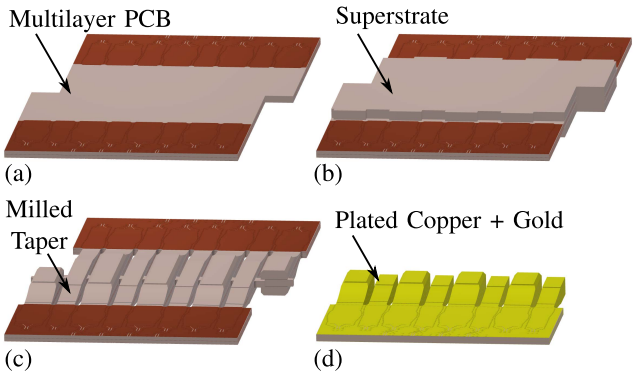

Fig. 16. Manufacturing steps of a submodule. (a) Multilayer PCB with (b) superstrates bonded, (c) SIW tapers milled, and (d) final metalization.

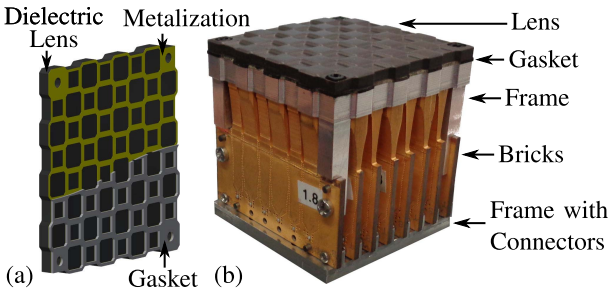

Fig. 17. (a) Backside of the lens with partial metallization and the gasket and (b) photograph of the assembled lens array.

sheet (*Nolato*'s *Compashield 8650*) by means of a laser cutter. Fig. 17(b) shows a photograph of the whole assembly.

B. Experimental Results

The scattering parameters are measured with a vector network analyzer (*ZVA50* from *Rohde & Schwarz*) after a thru-reflect-line (TRL) calibration at the CPW input. The radiation patterns are assessed in an anechoic chamber after calibration with the three-antenna method. Here, the reference planes are shifted to the polarizer inputs. To mitigate spurious reflections, the results are time-gated with a 0.9 m window.

1) Scattering Parameters: During Step 5 above, the coating partially covered some of the CPW gaps, thus altering their width. This affects the measurement accuracy, in particular, of the scattering parameters. Their reference plane had to be shifted to the CPWs instead of the polarizer inputs, as in the simulation, thus preventing a meaningful verification of the input reflection. The coupling coefficients, though, can still be roughly assessed, and the losses between the reference planes lower them by about 2–4 dB. Representative examples are reported below.

The coupling from the Rx/Tx port (16,**1**) to neighboring Rx/Tx ports is shown in Fig. 18(a). At port (16,**2**), it peaks at −15.7 dB in the *typical* frequency bands, which is up to 3 dB higher than simulated. The coupling to the elements 11 and 14 remains below −21.7 dB which is in good agreement with the simulated −19.3 dB. Similarly, Fig. 18(b) depicts the coupling between the Tx-only port (4,**1**) and neighboring ports. Again, the transmission is largest at port (4,**2**), where it reaches −15.6 dB, that is, up to 4 dB more than simulated. With at most −24.3 dB (−20 dB in simulation), the elements

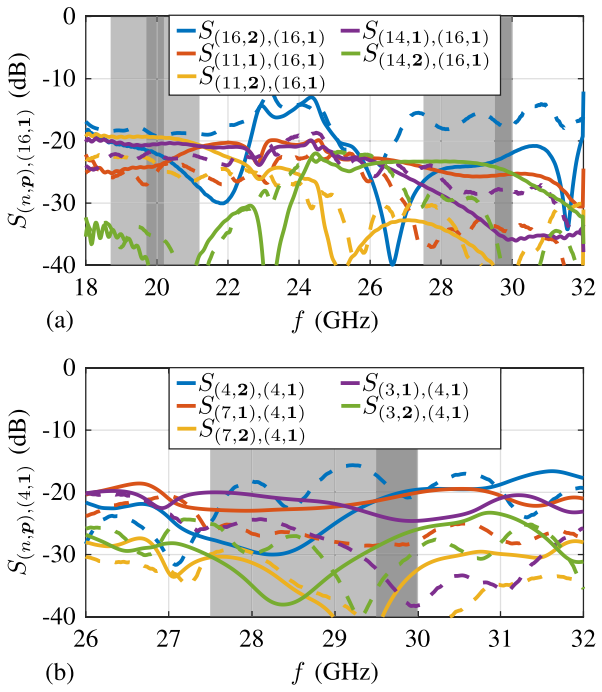

Fig. 18. (a) Coupling coefficients $S_{(n,p),(16,1)}$ and (b) $S_{(n,p),(4,1)}$ (▬ simulated, ▬ ▬ measured, ■ *typical*/■ *reference* bands).

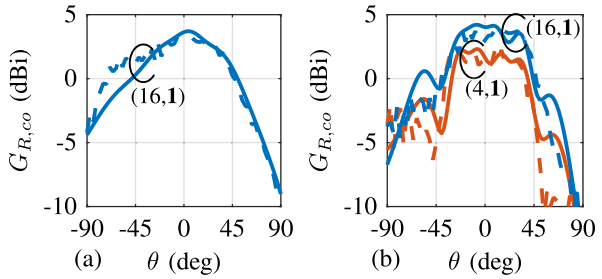

Fig. 19. Realized copolarized element gain $G_{R,co}$ in the xz-plane versus θ for (a) 20 and (b) 30 GHz (▬ Simulated and ▬ ▬ measured).

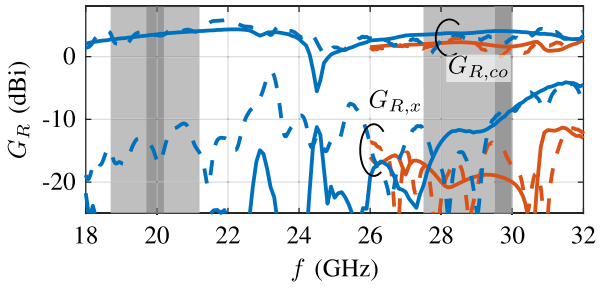

Fig. 20. Realized copolarized and cross-polarized element gain G_R in the boresight direction versus the frequency (▬ simulation, ▬ ▬ measurements, ▬ port (16, **1**), ▬ port (4, **1**), ■ *typical*/■ *reference* bands).

3 and 7 are only weakly coupled. In general, the coupling is acceptably low. The larger $S_{(n,2),(n,1)}$ values hint at a slightly misaligned septum, which is attributable to the manufacturing tolerances associated with this first realization.

2) Element Radiation Characteristics: The realized copolarized gain of elements (16,**1**) and (4,**1**) in Fig. 19 is representative. It reaches a few dB which is in good agreement with simulation, as plotted in the xz-plane versus θ at 20 and 30 GHz. In the Tx-band, the gain of these elements differs by about 2.5 dBi in the boresight direction, which is in the

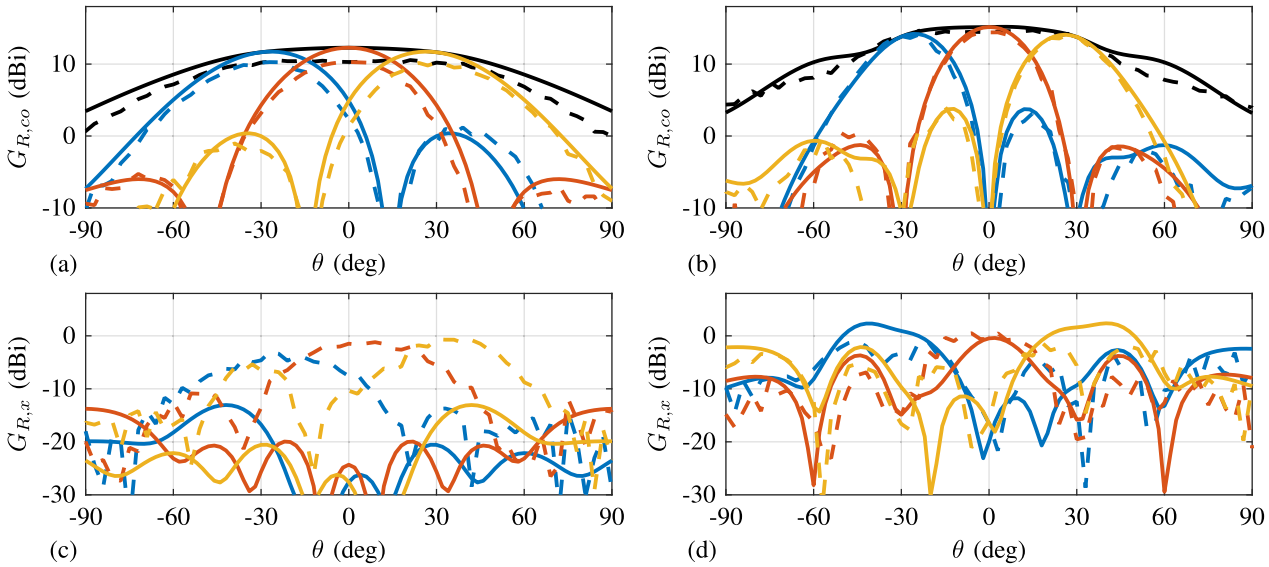

Fig. 21. Realized (a) and (b) copolarized and (c) and (d) cross-polarized gain G_R of the LHCP array pattern versus θ for (a) and (c) 20 GHz in the yz-plane and (b) and (d) 30 GHz in the xz-plane (— simulated, - - measured, — $\theta_0 = -30°$, — $\theta_0 = 0°$, — $\theta_0 = 30°$, — envelope).

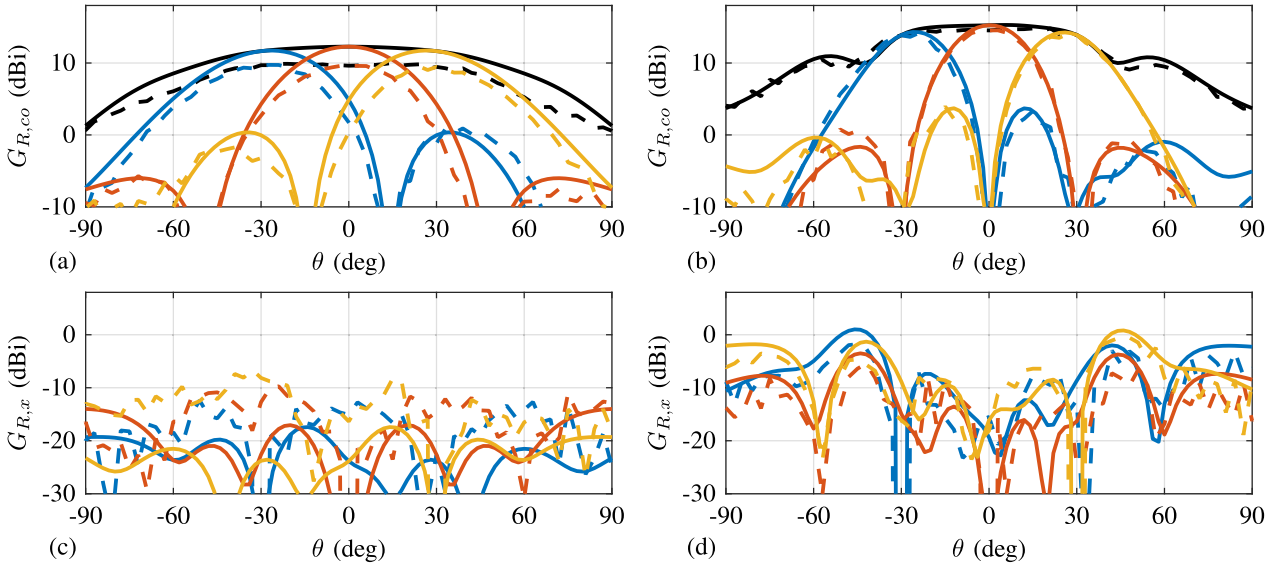

Fig. 22. Realized (a) and (b) copolarized and (c) and (d) cross-polarized gain G_R of the LHCP array pattern versus θ for (a) and (c) 20 GHz in the yz-plane and (b) and (d) 30 GHz in the xz-plane with polarization compensation (— simulated, - - measured, — $\theta_0 = -30°$, — $\theta_0 = 0°$, — $\theta_0 = 30°$, — envelope).

expected range, and their patterns exhibit a minimum at about $|\theta| = 45°$.

The frequency dependence is reported in Fig. 20. Whereas the measured copolarized gain essentially confirms the simulation, the cross-polarized one significantly exceeds the prediction in the Rx band. This is consistent with the observed increased coupling of the polarizer ports and, thus, most likely a manufacturing issue.

3) Array Radiation Characteristics Without Compensation: The LHCP and the RHCP array patterns are synthesized by superimposing the element characteristics. The port amplitudes are equal, and the phases are adjusted for constructive interference in the pointing direction (θ_0, ϕ_0). 2-D scanning is achieved for Rx and Tx with RHCP, LHCP, or even a user-defined polarization. Fig. 21 shows, as a representative example, the LHCP patterns for $(\theta_0, \phi_0) = (0°, 0°)$ and $(\pm 30°, 0°)$ in the yz-plane at 20 GHz and in the xz-plane at 30 GHz. They consistently reflect the effect of the array factor, except for Rx, where the measured gain is about 2 dB lower than simulated. This correlates with a reduced gain of the elements in the lower two submodules in Fig. 12(a). For these elements, the cross-polarization and the polarization port coupling $S_{(n,\mathbf{2}),(n,\mathbf{1})}$ are increased. This, in turn, is linked to the manufacturing issue of the polarizers mentioned previously. Fig. 21 additionally reports the maximum gain versus the pointing direction. The gain dip of the element patterns around $\pm 45°$ is reproduced as well, albeit less pronounced due to averaging effects. It could be due to surface modes in the lens. For $|\theta_0| \leq 30°$, the cross-polarization in the pointing direction translates into simulated (measured) axial ratios of up to 1.1 dB (5 dB) at 20 GHz and 4.3 dB (3.8 dB) at 30 GHz.

4) Array Radiation Patterns With Compensation: The simulated patterns in Fig. 22 demonstrate that, with the method discussed in Section II-D, the relatively high cross-polarization

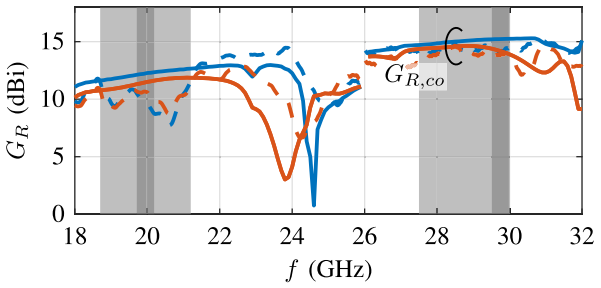

Fig. 23. Realized copolarized gain G_R of the LHCP array pattern in the pointing direction versus the frequency with polarization compensation (▬ simulated, ▬ ▬ measured, ▬ $\theta_0 = 0°$, ▬ $\theta_0 = 30°$, ▒ *typical*/▒ *reference* bands).

can be compensated in the pointing direction. Its level is generally reduced, except at 30 GHz around $|\theta| = 45°$ and for the experimental results at 20 GHz, where the cross-polarization is higher than simulated. The former is consistent with the assumed excitation of surface modes, and the latter with the manufacturing issues of the polarizers discussed above.

Fig. 23 shows the gain for $(\theta_0, \phi_0) = (0°, 0°)$ and $(30°, 0°)$ versus the frequency. In the *typical* Rx (Tx) bands, the simulated gain at boresight ranges between 11.6 and 12.7 dBi (14.7 and 15.3 dBi). At $(30°, 0°)$, it is about 1 dB less. For Tx, the measurements are in good agreement, but not for Rx, where the quite substantial differences confirm the previous findings.

5) Surface Area Comparison: The experimental results allow assessing the realizable aperture size reduction discussed in Section II-E. A diplexer such as in [40] exhibits losses of 0.7 and 1.2 dB in the Rx and the Tx path, respectively. Together with the simulated element losses in Fig. 13, this adds up to about 3.1 dB and 3.4 dB in the *reference* bands, respectively. The Tx-only element features a loss of about 3.3 dB. This is only slightly larger than the 3 dB assumed in Section II-E. Hence, separate arrays would be about 30% and, in the case of the mentioned ETSI limitations, even 50% larger than the integrated one.

V. Conclusion

The modular terminal antenna discussed in this work is intended for K-/Ka-band satellite communications. It is conceived as a passive, Rx/Tx integrated endfire array in brick architecture. It is composed of Tx-only and combined Rx/Tx elements featuring dual-circular polarization and arranged on an interleaved rectangular grid. The array is implemented in SIW technology. For improved matching, it is covered by a periodically shaped dielectric lens.

A 4×4 array, realized with standard technologies, serves as a demonstrator. To mitigate edge effects, it is embedded in an 8×8 array with terminated outer ports. Extensive measurements verify the functionality, in particular, dual-polarization in the *typical*, 2.5 GHz wide Rx and Tx bands. A proposed compensation technique is shown to significantly reduce cross-polarization around the pointing direction. A major result is a proof that the demonstrated Rx/Tx-integration saves between 30% and 50% surface area compared to the case of separate Rx and Tx arrays.

The experiments also reveal some manufacturing issues, which need to be remedied by optimizing the processes. Future work shall also address the observed surface wave effects to improve the scan angles. Finally, of course, a fully functional phased array and the realizable surface area savings shall be demonstrated.

References

[1] Eutelsat. (2010). *KA-SAT, Tooway Service*. [Online]. Available: www.eutelsat.com

[2] Inmarsat. (2013). *Inmarsat-5, Global Xpress Network*. [Online]. Available: www.inmarsat.com

[3] H. Fenech, S. Amos, A. Tomatis, and V. Soumpholphakdy, "High throughput satellite systems: An analytical approach," *IEEE Trans. Aerosp. Electron. Syst.*, vol. 51, no. 1, pp. 192–202, Jan. 2015.

[4] T. Lambard, O. Lafond, M. Himdi, H. Jeuland, S. Bolioli, and L. Le Coq, "Ka-band phased array antenna for high-data-rate SATCOM," *IEEE Antennas Wireless Propag. Lett.*, vol. 11, pp. 256–259, 2012.

[5] W. Theunissen, V. Jain, and G. Menon, "Development of a receive phased array antenna for high altitude platform stations using integrated beamformer modules," in *IEEE MTT-S Int. Microw. Symp. Dig.*, Jun. 2018, pp. 779–782.

[6] A. H. Aljuhani, T. Kanar, S. Zihir, and G. M. Rebeiz, "A 256-element Ku-band polarization agile SATCOM receive phased array with wide-angle scanning and high polarization purity," *IEEE Trans. Microw. Theory Techn.*, vol. 69, no. 5, pp. 2609–2628, May 2021.

[7] K. K. W. Low, S. Zihir, T. Kanar, and G. M. Rebeiz, "A 27–31-GHz 1024-element Ka-band SATCOM phased-array transmitter with 49.5-dBW peak EIRP, 1-dB AR, and ±70° beam scanning," *IEEE Trans. Microw. Theory Techn.*, vol. 70, no. 3, pp. 1757–1768, Mar. 2022.

[8] K. K. W. Low, T. Kanar, S. Zihir, and G. M. Rebeiz, "A 17.7–20.2-GHz 1024-element K-band SATCOM phased-array receiver with 8.1-dB/K G/T, ±70° beam scanning, and high transmit isolation," *IEEE Trans. Microw. Theory Techn.*, vol. 70, no. 3, pp. 1769–1778, Mar. 2022.

[9] E. Arnieri, L. Boccia, and G. Amendola, "A Ka-band dual-frequency radiator for array applications," *IEEE Antennas Wireless Propag. Lett.*, vol. 8, pp. 894–897, 2009.

[10] T. Jaschke, B. Rohrdantz, H. K. Mitto, and A. F. Jacob, "Rx/Tx integration concepts for ground segment SatCom antenna arrays," in *Proc. German Microw. Conf. (GeMiC)*, Mar. 2016, pp. 27–30.

[11] R. J. Mailloux, "Antenna array architecture," *Proc. IEEE*, vol. 80, no. 1, pp. 163–172, Jan. 1992.

[12] Q. Luo et al., "Antenna array elements for Ka-band satellite communication on the move," in *Proc. Loughborough Antennas Propag. Conf. (LAPC)*, Nov. 2013, pp. 135–139.

[13] T. Chaloun, C. Waldschmidt, and W. Menzel, "Wide-angle scanning cavity antenna element for mobile satcom applications at Ka band," in *Proc. 10th Eur. Conf. Antennas Propag. (EuCAP)*, Apr. 2016, pp. 1–5.

[14] A. I. Sandhu, E. Arnieri, G. Amendola, L. Boccia, E. Meniconi, and V. Ziegler, "Radiating elements for shared aperture Tx/Rx phased arrays at K/Ka band," *IEEE Trans. Antennas Propag.*, vol. 64, no. 6, pp. 2270–2282, Jun. 2016.

[15] Z.-J. Guo, Z.-C. Hao, H.-Y. Yin, D.-M. Sun, and G. Q. Luo, "Planar shared-aperture array antenna with a high isolation for millimeter-wave low earth orbit satellite communication system," *IEEE Trans. Antennas Propag.*, vol. 69, no. 11, pp. 7582–7592, Nov. 2021.

[16] F. Greco, G. Amendola, E. Arnieri, L. Boccia, and A. I. Sandhu, "A dual-band, dual-polarized array element for Ka band satcom on the move terminals," in *Proc. 8th Eur. Conf. Antennas Propag. (EuCAP)*, Apr. 2014, pp. 2432–2435.

[17] B. Rohrdantz, T. Jaschke, F. K. H. Gellersen, and A. F. Jacob, "A dual-frequency and dual-polarized patch antenna at Ka-band," in *Proc. Eur. Microw. Conf. (EuMC)*, Sep. 2015, pp. 1495–1498.

[18] B. Rohrdantz, T. Jaschke, F. K. H. Gellersen, A. Sieganschin, and A. F. Jacob, "Ka-band antenna arrays with dual-frequency and dual-polarized patch elements," *Int. J. Microw. Wireless Technol.*, vol. 8, no. 6, pp. 963–972, Sep. 2016.

[19] S. S. Holland, D. H. Schaubert, and M. N. Vouvakis, "A 7–21 GHz dual-polarized planar ultrawideband modular antenna (PUMA) array," *IEEE Trans. Antennas Propag.*, vol. 60, no. 10, pp. 4589–4600, Oct. 2012.

[20] J. T. Logan and M. N. Vouvakis, "Planar ultrawideband modular antenna (PUMA) arrays scalable to mm-waves," in *Proc. IEEE Antennas Propag. Soc. Int. Symp. (APSURSI)*, Jul. 2013, pp. 624–625.

[21] R. J. Bolt et al., "Characterization of a dual-polarized connected-dipole array for Ku-band mobile terminals," *IEEE Trans. Antennas Propag.*, vol. 64, no. 2, pp. 591–598, Feb. 2016.
[22] K. Trott, B. Cummings, R. Cavener, M. Deluca, and J. Biondi, "7–21 GHz wideband phased array radiator," in *Proc. IEEE Antennas Propag. Symp.*, vol. 3, Jun. 2004, pp. 2265–2268.
[23] S. Lee, "Aperture matching for an infinite circular polarized array of rectangular waveguides," *IEEE Trans. Antennas Propag.*, vol. AP-19, no. 3, pp. 332–342, May 1971.
[24] C.-C. Chen, "Wideband wide-angle impedance matching and polarization characteristics of circular waveguide phased arrays," *IEEE Trans. Antennas Propag.*, vol. AP-22, no. 3, pp. 414–418, May 1974.
[25] G. Tsandoulas and G. Knittel, "The analysis and design of dual-polarization square-waveguide phased arrays," *IEEE Trans. Antennas Propag.*, vol. AP-21, no. 6, pp. 796–808, Nov. 1973.
[26] K. Kuhlmann, K. Rezer, and A. F. Jacob, "Circularly polarized substrate-integrated waveguide antenna array at Ka-band," in *Proc. German Microw. Conf. (GeMiC)*, 2008, pp. 471–474.
[27] K. Kuhlmann and A. F. Jacob, "Active 30 GHz antenna array for digital beamforming and polarization multiplexing," in *IEEE MTT-S Int. Microw. Symp. Dig.*, May 2010, pp. 1276–1279.
[28] D. F. Filipovic, S. S. Gearhart, and G. M. Rebeiz, "Double-slot antennas on extended hemispherical and elliptical silicon dielectric lenses," *IEEE Trans. Microw. Theory Techn.*, vol. 41, no. 10, pp. 1738–1749, Oct. 1993.
[29] B. Chantraine-Bares and R. Sauleau, "Electrically-small shaped integrated lens antennas: A study of feasibility in *Q*-band," *IEEE Trans. Antennas Propag.*, vol. 55, no. 4, pp. 1038–1044, Apr. 2007.
[30] T. Jaschke, B. Rohrdantz, and A. F. Jacob, "A flexible surface description for arbitrarily shaped dielectric lens antennas," in *Proc. German Microw. Conf. (GeMiC)*, 2014, pp. 1–4.
[31] T. Jaschke, B. Rohrdantz, and A. F. Jacob, "A flexible surface description for arbitrarily shaped dielectric lens antennas," *Frequenz*, vol. 69, nos. 1–2, pp. 29–37, 2015.
[32] T. Jaschke, H. K. Mitto, and A. F. Jacob, "An SIW fed dual-band and dual-polarized lens antenna at K/Ka-band," in *Proc. 47th Eur. Microw. Conf. (EuMC)*, Oct. 2017, pp. 62–65.
[33] T. Jaschke, B. Rohrdantz, H. K. Mitto, and A. F. Jacob, "Ultrawideband SIW-fed lens antenna," *IEEE Antennas Wireless Propag. Lett.*, vol. 16, pp. 2010–2013, 2017.
[34] T. Jaschke, H. K. Mitto, and A. F. Jacob, "K/Ka-band dual-polarized SIW-fed lens antennas for Rx/Tx integration," *Int. J. Microw. Wireless Technol.*, vol. 10, pp. 627–634, Jun. 2018.
[35] R. S. Hao, J. F. Zhang, S. C. Jin, D. G. Liu, T. J. Li, and Y. J. Cheng, "K/Ka-band shared-aperture phased array with wide bandwidth and wide beam coverage for LEO satellite communication," *IEEE Trans. Antennas Propag.*, early access, Nov. 18, 2022, doi: 10.1109/TAP.2022.3222091.
[36] M. Chen and G. Tsandoulas, "A wide-band square-waveguide array polarizer," *IEEE Trans. Antennas Propag.*, vol. AP-21, no. 3, pp. 389–391, May 1973.
[37] J. Esteban and J. M. Rebollar, "Field theory CAD of septum OMT-polarizers," in *Proc. IEEE Antennas Propag. Soc. Int. Symp.*, vol. 4, Jun. 1992, pp. 2146–2149.
[38] R. Ihmels, U. Papziner, and F. Arndt, "Field theory design of a corrugated septum OMT," in *IEEE MTT-S Int. Microw. Symp. Dig.*, Jun. 1993, pp. 909–912.
[39] A. Sieganschin, T. Jaschke, D. Safi, and A. F. Jacob, "On the design of active Rx/Tx-diplexers with wide frequency spread," in *Proc. 11th German Microw. Conf. (GeMiC)*, Mar. 2018, pp. 1–4.
[40] A. Sieganschin, T. Jaschke, H. K. Mitto, N. J. Lamann, J. Waldhelm, and A. F. Jacob, "A compact low-loss multilayer SIW diplexer at K/Ka-band," in *Proc. 12th German Microw. Conf. (GeMiC)*, Mar. 2019, pp. 51–54.
[41] A. Sieganschin, T. Jaschke, and A. F. Jacob, "A compact diplexer for circularly polarized 20/30 GHz SIW-antennas," in *IEEE MTT-S Int. Microw. Symp. Dig.*, Aug. 2020, pp. 1–4.
[42] A. Sieganschin, T. Jaschke, and A. F. Jacob, "A compact low-noise frontend for Rx/Tx-integrated SatCom arrays," in *Proc. 50th Eur. Microw. Conf. (EuMC)*, Jan. 2021, pp. 1–4.
[43] A. Sieganschin, T. Jaschke, and A. F. Jacob, "A compact low-noise frontend for interleaved Rx/Tx arrays at K-/Ka-band," *Int. J. Microw. Wireless Technol.*, vol. 13, no. 6, pp. 595–601, Jul. 2021.
[44] A. Sieganschin, T. Jaschke, J. Waldhelm, N. J. Lamann, and A. F. Jacob, "A K/Ka-band front-end for dual-beam, dual-polarized Tx/Rx phased arrays," in *Proc. 51st Eur. Microw. Conf. (EuMC)*, Apr. 2022, pp. 192–195.
[45] L. Hogben, *Handbook of Linear Algebra* (Discrete Mathematics and its Applications), 2nd ed. Boca Raton, FL, USA: CRC Press, 2016.
[46] *Satellite Earth Stations and Systems (SES); Harmonised Standard for Earth Stations on Mobile Platforms (ESOMP)*, document ETSI EN 302 978, V2.1.2, 2016.
[47] D. M. Pozar, *Microwave Engineering*, 4th ed. Hoboken, NJ, USA: Wiley, 2012.
[48] D. F. Rogers, *An Introduction to NURBS: With Historical Perspective*. San Francisco, CA, USA: Morgan Kaufmann, 2001.
[49] X.-P. Chen and K. Wu, "Low-loss ultra-wideband transition between conductor-backed coplanar waveguide and substrate integrated waveguide," in *IEEE MTT-S Int. Microw. Symp. Dig.*, Jun. 2009, pp. 349–352.
[50] T. Jaschke and A. F. Jacob, "Novel multilayer SIW tapers synthesized using an extended transverse resonance method," in *IEEE MTT-S Int. Microw. Symp. Dig.*, Jun. 2017, pp. 715–718.

Thomas Jaschke was born in Hamburg, Germany, in 1988. He received the B.Sc. and M.Sc. degrees from the Hamburg University of Technology, Hamburg, Germany, in 2010 and 2012, respectively, and the Ph.D. degree from the Institute of High-Frequency Technology, Hamburg University of Technology, in 2021.

Since 2020, he has been a Radar System Engineer with Wärtsilä Voyage GmbH, Hamburg. His current research interests include active radar systems, phased arrays, passive components, electromagnetic theory, and antenna measurements.

Arne F. Jacob (Life Fellow, IEEE) received the Dr.-Ing. degree from Technische Universität Braunschweig, Braunschweig, Germany, in 1986.

From 1986 to 1988, he was a fellow at CERN, the European Organization for Nuclear Research, Geneva, Switzerland. In 1988, he joined the Lawrence Berkeley (National) Laboratory, University of California at Berkeley, Berkeley, CA, USA, for almost three years as a Staff Scientist with the Accelerator and Fusion Research Division. In 1990, he became a Professor at the Institut für Hochfrequenztechnik, Technische Universität Braunschweig. From 2004 until his retirement in April 2020, he was a Professor and the Head of the Institute of High-Frequency Technology, Hamburg University of Technology, Hamburg, Germany. His current research interests include the design, packaging, and application of integrated (sub)systems up to millimeter-wave frequencies and the characterization of complex materials.